PCCP

PAPER

View Article Online
View Journal | View Issue

Cite this: *Phys. Chem. Chem. Phys.*, 2024, **26**, 10841

Two-dimensional fullerene-based monolayer materials assembled by C_{80} and $Sc_3N@C_{80}$†

Yang Zhao,[a] Yu Guo,[a] Yanyan Zhao,[a] Xueke Yu,[a] Nikolai Cherenda,[b] Yan Su *[a] and Jijun Zhao *[a]

Construction of two-dimensional (2D) materials using fullerenes as building blocks has attracted particular attention, primarily due to their ability to integrate desired functionalities into devices. However, realization of stable 2D phases of polymerized fullerenes remains a big challenge. Here, we propose two stable 2D monolayer phases with covalently bridged C_{80} cages, namely α-C_{80}-2D and β-C_{80}-2D, which are semiconductors with strong absorption in the long wave range and appreciable carrier mobility, respectively. The high stability originates from the bond energy released by the [2+2] cycloaddition polymerization of C_{80} is greater than the deformation energy of a cage. Starting from α-C_{80}-2D, endohedral incorporation of the Sc_3N molecule into each C_{80} cage leads to 2D semiconductors of α-$Sc_3N@C_{80}$-2D and α'-$Sc_3N@C_{80}$-2D, which possess exceptional stability and diverse physical properties, including unique electronic band structures, strong optical absorption in the visible (VIS) to near-infrared (NIR) regime, and anisotropic optical characteristics. Remarkably, a temperature-induced order–disorder transition in the α-$Sc_3N@C_{80}$-2D phase has been observed at elevated temperatures above 600 K. These findings expand the family of 2D carbon materials and provide useful clue for the potential applications of fullerene-assembled monolayer networks.

Received 22nd August 2023,
Accepted 23rd February 2024

DOI: 10.1039/d3cp04028c

rsc.li/pccp

1. Introduction

Owing to the stable cage structure and unique physical and chemical properties, carbon fullerenes are ideal building blocks of novel functional materials. To date, various fullerenes of different sizes, such as C_{60} and C_{70}, have been successfully synthesized in bulk amounts.[1–4] In addition, the interior cavity of fullerene cages provides ideal space for hosting atoms or small clusters, forming endohedral carbon fullerenes.[5–7] To this end, the discovery of $Sc_3N@I_h$–C_{80} with high yields and high stability marks a breakthrough in the study of endohedral metallofullerenes.[8] The interaction between guest atoms or clusters and host carbon cages may give rise to novel properties and lead to potential applications in single-molecule electronics and information storage, quantum computing, biomedicine, nanocatalysis, and so on. For example, two electric dipole states switched by external electric fields and single-molecule ferroelectric effects have been observed in $Gd@C_{82}$, which can be considered as a prototype of atomic-scale storage and logic devices.[9] $Sc_2C_2@C_s$(hept)–C_{88} can be used as a two-terminal single-metallofullerene device achieving room-temperature logic-in-memory operations.[10] $U_2C@C_{80}$–M (M = Cr, Mn, Mo, and Ru) chains, which exhibit intrinsic multiferroic behavior, are promising one-dimensional materials for the realization of a novel multifunctional device.[11] $Gd@C_{82}$ nanoparticles have been demonstrated to trigger robust cancer immunotherapy and relieve fatty liver disease without obvious toxicity.[12,13] The 1T-MoS_2/C_{60} heterostructure is an excellent electrocatalyst for the hydrogen evolution reaction.[14]

Recently, two-dimensional (2D) polymerized C_{60} monolayer structures have been fabricated *via* covalent C–C bonds, which not only enrich the family of carbon fullerene derivatives but also bring new opportunities in fullerene-based materials and devices.[15] This exciting breakthrough has led to boom of C_{60}-based 2D structures. For instance, Zheng *et al.* synthesized a covalently bonded monolayer polymeric C_{60} with high crystallinity, good thermodynamic stability and moderate band gap.[15] Using α-Li_3N to catalyze C_{60} powder at ambient pressure, Zhu *et al.* obtained gram-scale long-range ordered porous carbon.[16] At the same time, Roy *et al.* reported van der Waals C_{60} polymer materials with ultra-clean surfaces and found that their thermal conductivity was much higher than that of the C_{60} molecule.[17] The unique geometric and electronic structures of 2D polymeric C_{60} monolayer materials endow them with great

[a] *Key Laboratory of Materials Modification by Laser, Ion and Electron Beams (Dalian University of Technology), Ministry of Education, Dalian 116024, China. E-mail: su.yan@dlut.edu.cn, zhaojj@dlut.edu.cn*
[b] *Physics Faculty, Belarusian State University, Minsk 220030, The Republic of Belarus*

† Electronic supplementary information (ESI) available. See DOI: https://doi.org/10.1039/d3cp04028c

promise in optoelectronics, spintronics, information and energy storage, and photocatalysis.[18–21]

As the smallest fullerene obeying the isolated pentagonal ring (IPR) rule,[22] C_{60} has relatively narrow interior space and can only enclose small guest species. In the fullerene family, C_{80} is the next member obeying the IPR rule and shares the same I_h point group symmetry with C_{60}.[23] Compared to C_{60}, the larger cavity of I_h–C_{80} cages allows hosting a variety of molecules or clusters with up to seven atoms, *e.g.*, $Sc_4CHN@I_h(7)$–C_{80}, $Sc_4C_2H@I_h(7)$–C_{80}, and $Sc_4O_3@I_h(7)$–C_{80}.[24–28] Therefore, it would be desirable to assemble novel crystals of different dimensionality using I_h–C_{80} and its endohedral derivatives as building blocks, which are expected to possess tunable electronic, magnetic, and optical properties.

Inspired by the recent breakthrough in 2D polymeric C_{60} crystals, in this paper, we propose two thermodynamically and dynamically stable 2D phases of polymerized C_{80}, *i.e.*, central rectangular (α-C_{80}-2D) and hexagonal porous (β-C_{80}-2D) lattice structures, which are indirect semiconductors and direct semiconductors with appreciable carrier mobility and strong absorption in the long wave range, respectively. Covalent polymerization of endohedral fullerene $Sc_3N@C_{80}$ leads to two kinds of 2D semiconductors with central rectangular lattice structures (denoted as α-$Sc_3N@C_{80}$-2D and α'-$Sc_3N@C_{80}$-2D), which are bistable states with distinct electronic band structures. A temperature-controlled order–disorder transition is observed in α-$Sc_3N@C_{80}$-2D at high temperatures above 600 K. These theoretical findings provide valuable insights into the development of fullerene-based 2D materials and devices.

2. Computational details

All individual fullerenes and fullerene-based 2D networks were optimized using the Vienna ab initio simulation package[29,30] (VASP) with the Perdew–Burke–Ernzerhof (PBE) exchange–correlation functional.[31] The electron–ion interaction was described using projector augmented wave (PAW) potential,[32] and the plane-wave basis set was expanded to 500 eV. In order to account for the strong Coulomb interaction of 3d electrons in Sc atoms, an effective Hubbard parameter, $U_{eff} = U - J = 3$ eV, was applied to Sc atoms, where U represents the Coulomb repulsion and J is the exchange parameter (Table S1, ESI†).[33–36] The introduction of U_{eff} parameters can more accurately describe the electronic properties of the system. A $30 \times 30 \times 30$ Å^3 supercell was utilized to simulate the isolated fullerene, and a Γ point was used to sample the Brillouin zone. Based on the PBE-optimized equilibrium structures, the more accurate electronic band structures and optical absorption spectra were calculated using the Heyd–Scuseria–Ernzerhof (HSE06) hybrid functional[37] with VASP. The deformation energy (E_d) of C_{80} or $Sc_3N@C_{80}$ in the 2D polymeric phase (α-C_{80}, β-C_{80} or α-$Sc_3N@C_{80}$ and α'-$Sc_3N@C_{80}$ cages) relative to the isolated one (C_{80} or $Sc_3N@C_{80}$) is defined as follows:

$$E_d = E_{2D\text{-def-cage}} - E_{C_{80}/Sc_3N@C_{80}} \quad (1)$$

where $E_{2D\text{-def-cage}}$ and $E_{C_{80}/Sc_3N@C_{80}}$ are the energies of the deformed cage in 2D structures and the standalone cage in its ground state configuration, respectively.

For fullerene-based 2D networks, a vacuum space with a 35 Å thickness was added to ensure separation between neighboring layers. A series of k-meshes of $2 \times 3 \times 1$ (for central rectangular lattice), $2 \times 2 \times 1$ (for hexagonal porous lattice), $4 \times 4 \times 1$ (for rectangular lattice) and $4 \times 1 \times 2$ (for α'-$Sc_3N@C_{80}$-2D) were used to sample the 2D Brillouin zones. During geometry optimization, atomic positions were allowed to relax until the maximum force was below 10^{-2} eV Å^{-1} and the change in total energy was less than 10^{-4} eV, respectively. The average C–C bond energy (E_b) is defined as follows:

$$E_b = (E_{2D} - N \times E_{2D\text{-cage}})/n \quad (2)$$

where E_{2D} is the energy of the 2D monolayer, N is the number of cages in the unit cell, $E_{2D\text{-cage}}$ is the energies of the deformed cages in 2D structures, and n is the number of C–C bonds between neighboring fullerene cages in the unit cell.

To further assess the thermal stability of these fullerene-based 2D networks, the formation energy (E_f) is calculated as follows:

$$E_f = (E_{2D} - N \times E_{cage})/N \quad (3)$$

where E_{2D} and E_{cage} are the energies of the 2D monolayer and isolated C_{80} or $Sc_3N@C_{80}$ cages, respectively. To assess the thermal and dynamical stabilities of these 2D fullerene networks, *ab initio* molecular dynamics (AIMD)[38] simulations within the *NVT* canonical ensemble were carried out for up to 10 ps with a time step of 2 fs, and phonon dispersions were calculated using the density functional perturbation theory implemented in the Phonopy software.[39]

3. Results and discussion

3.A. Structures and stabilities of 2D monolayer polymeric C_{80}

To explore the possible stable configurations of 2D networks composed of C_{80} fullerenes, we consider three different connecting manners: a central rectangular lattice, a hexagonal porous lattice, and a rectangular lattice. The optimized structures are depicted in Fig. 1(a) and (b) and Fig. S1 (ESI†), and detailed geometrical parameters are provided in Table 1. Among these three constructed phases, the α-C_{80}-2D monolayer with the *Pmna* (No. 53) space group and equilibrium lattice parameters of a = 17.76 Å and b = 10.25 Å is the most stable, in which each C_{80} cage is linked by six neighboring C_{80} cages through [2+2] cycloaddition bonds along the b direction and the diagonal lines of the rectangular unit cell. For comparison, the equilibrium structure of the β-C_{80}-2D network exhibits the $P\bar{3}m1$ (No. 164) space group with lattice parameters of a = 17.64 Å and b = 17.64 Å, which is achieved through the formation of similar plane [2+2] cycloaddition bonds involving three adjacent fullerenes. For the γ-C_{80}-2D network with the space group of $P\bar{1}$ (No. 2), the equilibrium lattice parameters are a = 10.19 Å and b = 9.90 Å, in which four fullerenes are

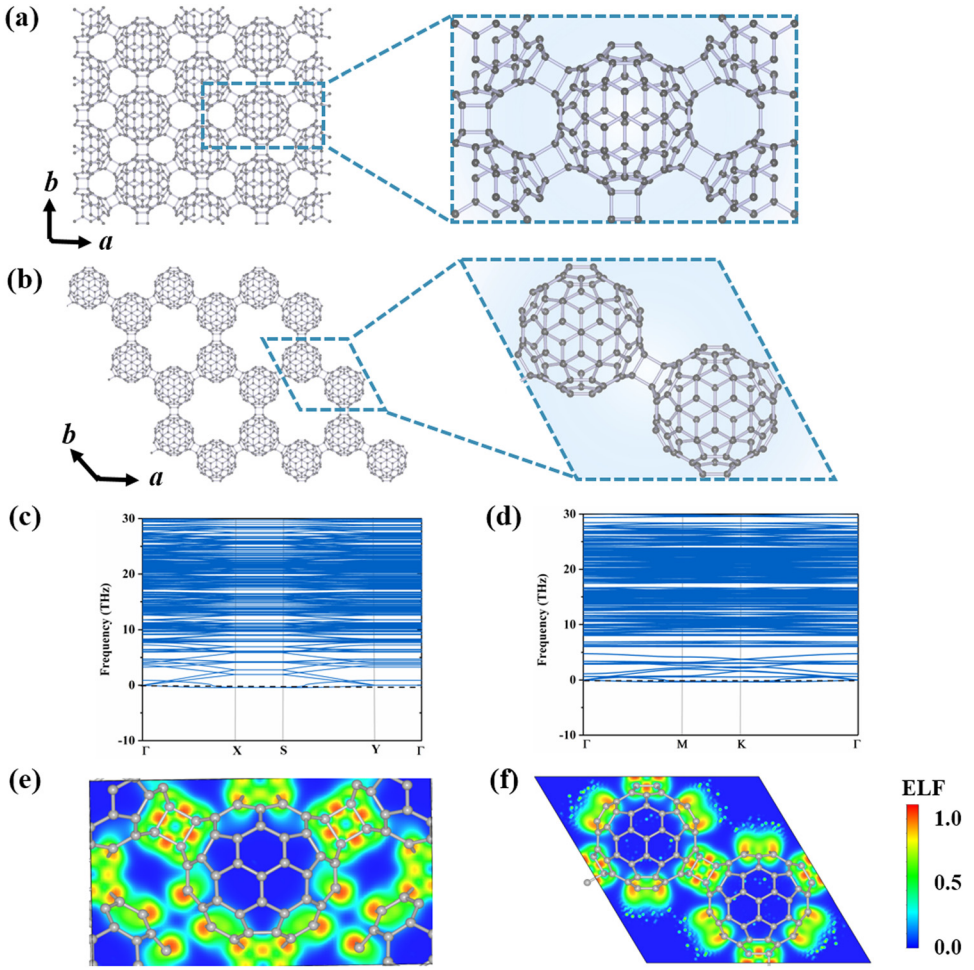

Fig. 1 Crystal structures of polymeric C_{80} monolayer phases: (a) α-C_{80}-2D and (b) β-C_{80}-2D. Phonon dispersion of (c) α-C_{80}-2D and (d) β-C_{80}-2D. Contour plots of ELFs for (e) α-C_{80}-2D through the (010) plane and (f) β-C_{80}-2D through the (001) plane, respectively. The ELF value indicates the degree of electron localization with values ranging from 0 (complete delocalization) to 1 (complete localization).

Table 1 Geometric parameters and key electronic properties of 2D monolayers, including space groups, lattice constants (a, b/c), the number of inter-cage C–C bonds (n) and the corresponding bond lengths (R_{C-C}), deformation energy (E_d), average C–C bond energy (E_b), formation energy (E_f), and electronic bandgaps (E_g)

Monolayer	Space group	a (Å)	b/c (Å)	n	R_{C-C} (Å)	E_d (eV)	E_b (eV)	E_f (eV)	E_g (eV)
qTP-C_{60}	*Pmmm* (47)	8.70	9.00	8	1.58/1.58	4.75	−0.89	−2.39	1.68
qHP-C_{60}	*Pmna* (53)	15.70	8.50	8	1.58/1.59	5.30	−1.95	−2.49	1.43
α-C_{80}-2D	*Pmna* (53)	17.76	10.25	12	1.59/1.60	7.41	−2.01	−4.66	0.14
β-C_{80}-2D	$P\bar{3}m1$(164)	17.64	17.64	6	1.59/1.60	3.14	−1.85	−2.41	0.25
γ-C_{80}-2D	$P\bar{1}$(2)	10.19	9.90	8	1.62/1.76	5.59	−0.97	−2.16	0.73
α-Sc_3N@C_{80}-2D	*Pma*2 (28)	17.88	10.31	12	1.58/1.60	6.07	−1.36	−2.08	0.36
α'-Sc_3N@C_{80}-2D	*Pc* (7)	10.23	20.50	12	1.59/1.62	6.60	−1.48	−2.29	0.12

connected by two [2+2] cycloaddition bonds along the a direction and C–C single bonds along the b direction.

As summarized in Table 1, the calculated formation energies of the α-C_{80}-2D, β-C_{80}-2D, and γ-C_{80}-2D monolayers are −4.66, −2.41, and −2.16 eV, respectively. These negative values indicate that synthesis of all three 2D structures from C_{80} cages is exothermic. For comparison, we have also calculated the formation energies of previously reported qTP-C_{60} and qHP-C_{60}.[18] Notably, our predicted α-C_{80}-2D network has much lower formation energy than 2D polymeric C_{60} crystals, while β-C_{80}-2D is only slightly less stable than qHP C_{60} by 0.08 eV per cage. Additionally, we also calculate the formation energy ($E_{f\text{-atom}}$) and deformation energy ($E_{d\text{-atom}}$) defined by atom-wise energies and compared with monolayer C_{60} (see Supplementary Note 2 of the ESI†). From Table S2 (ESI†), it can be seen that the thermodynamic stability of the C_{80}-2D monolayer is

comparable to that of the C_{60}-2D monolayer. Therefore, these 2D networks composed of C_{80} fullerenes would be accessible under experimental conditions.

The phonon dispersions of the three C_{80}-assembled 2D monolayers are computed and illustrated in Fig. 1(c) and (d) and Fig. S1 (ESI†). Among them, the α-C_{80}-2D, β-C_{80}-2D and γ-C_{80}-2D monolayers exhibit dynamic stability without imaginary frequencies in the entire phonon spectra. Furthermore, AIMD simulations, as presented by Fig. S3 (ESI†), demonstrate that α-C_{80}-2D and β-C_{80}-2D monolayers maintain their lattice structures at temperatures as high as 600 K. However, in the γ-C_{80}-2D monolayer, there is a noticeable increase in C–C distances along the b direction within the 2D structure (Fig. S4, ESI†). According to the aforementioned results, α-C_{80}-2D and β-C_{80}-2D monolayers exhibit excellent dynamic and thermal stabilities, making them viable candidates for experimental synthesis and excellent ''host'' materials for further endohedral doping.

To elucidate the exceptional stability of polymeric C_{80} monolayers, we analyze their bonding characteristic in terms of electron localization functions (ELFs), average inter-cage C–C bond energy (E_b), orbital-resolved partial density of state (PDOS) and deformation energy (E_d). Fig. 1(e) and (f) reveal high electron localization and strong covalent bonding between neighboring C_{80} cages in both α-C_{80}-2D and β-C_{80}-2D. This picture is further supported by the calculated E_b in Table 1. Fig. S5 (ESI†) presents the orbital-resolved partial density of states (PDOS) of C_{80}-based 2D polymers. It is evident that the p_x, p_y, and p_z orbitals of the C atoms all contribute equally to bonding, implying a transition of the part of the C atoms in C_{80} fullerenes from sp^2 to sp^3 hybridization. Intuitively, as more C atoms reach sp^3 bonding saturation through inter-cage polymerization, a greater amount of surface tension is released in the originally unstable C_{80} cage,[23,40] further increasing the stability of the entire system. As seen from Fig. 1(a) and (b) and Table 1, compared with C_{60} polymeric 2D materials like qTP-C_{60} and qHP-C_{60},[18] each fullerene cage in α-C_{80}-2D has 12 C atoms with sp^3-hybridization by [2+2] cycloaddition with the surrounding six fullerenes. Although the deformation energy of the C_{80} cage is relatively larger (E_d) (Fig. S6, ESI†), this effect is compensated by the number of saturated bonds in the carbon cage, as signified by the amount of bond energy (nE_b). As a consequence, α-C_{80}-2D exhibits a significantly lower formation energy of -4.66 eV than C_{60}-based 2D phases. For β-C_{80}-2D, each carbon cage possesses 6 C atoms with sp^3 hybridization, slightly less than the number in qTP-C_{60} or qHP-C_{60}, while the deformation energy of the cage is also smaller. However, for the γ-C_{80}-2D monolayer, each C_{80} cage contains 8 C atoms with sp^3-hybridization, but the C–C bond length (1.76 Å) is 0.16 Å longer than that formed through [2+2] cycloaddition, resulting in a weaker average inter-cage C–C bond energy. While compared to the relatively large cage deformation energy, the bond energy release is only slightly increased, leading to the relative inferior stability of γ-C_{80}-2D. According to the above analysis, the bond energy released by the [2+2] cycloaddition polymerization of C_{80} is consistently greater than the deformation energy of the cage, contributing to the stabilization of the resulting 2D phases. In summary, theoretical calculations suggest that C_{80} could serve as a promising building block to construct C_{60}-2D-like monolayers. Additionally, we aspire for this study to inspire more theoretical and experimental efforts towards the synthesis of C_{80} monolayers.

3.B. Enclosing Sc_3N into 2D C_{80} polymerized monolayers

The incorporation of endohedral units into C_{80} fullerene provides an extra opportunity for designing multifunctional nanodevices.[11,41–43] According to previous reports, the Sc_3N@I_h–C_{80} cluster shows great potential in various fields such as biomedicine and energy conversion.[44,45] Based on the stable C_{80}-assembled monolayer phases obtained above (*i.e.*, central rectangular and hexagonal porous lattices), we select Sc_3N as the guest species inside the C_{80} cage to further construct Sc_3N@C_{80}-2D monolayers.

To determine the stable geometries of Sc_3N@C_{80}-2D monolayers, we have explored various possible orientations of the Sc_3N cluster in α-C_{80}-2D and β-C_{80}-2D phases. As illustrated in Fig. 2(a) and (b), α'-Sc_3N@C_{80}-2D and α-Sc_3N@C_{80}-2D monolayers are the most stable and metastable phases, respectively. The phonon dispersions of these two phases are displayed in Fig. 2(c) and (d). Notably, in the α-Sc_3N@C_{80}-2D crystal (Fig. 2(a)), the central rectangular lattice is maintained after endohedral doping, with equilibrium lattice parameters of a = 17.88 Å and b = 10.31 Å, and a space group of *Pma*2 (No. 28). Intriguingly, the formation energy of this phase (-2.08 eV) is significantly lower than those of polymeric C_{80} and C_{60} crystals, suggesting that incorporation of the Sc_3N cluster effectively passivates the surface activity of the fullerene cage and further reduces the average C–C bond energy (Table 1). These results demonstrate the experimental feasibility of synthesizing α-Sc_3N@C_{80}-2D and α'-Sc_3N@C_{80}-2D monolayers. In both the freestanding cage and α-Sc_3N@C_{80}-2D, the geometry of the endohedral Sc_3N cluster retains a N-centered equilateral triangle with minor distortion (Fig. S7(a), ESI†). In the α-Sc_3N@C_{80}-2D phase, the Sc–N bond lengths are 2.04, 2.04, and 2.04 Å, slightly longer than those in isolated Sc_3N@C_{80}, *i.e.*, 2.02, 2.02, and 2.02. All three Sc atoms are located over the [5, 6] junction of the I_h–C_{80} cage in α-Sc_3N@C_{80}-2D (Fig. S7(a), ESI†). For the α'-Sc_3N@C_{80}-2D crystal, the lattice parameters are a = 10.23 Å and c = 20.50 Å, with a space group of *Pc* (No. 7). The formation energy of -2.29 eV indicates slightly higher stability compared to the α-Sc_3N@C_{80}-2D phase. The enclosed Sc_3N species in α'-Sc_3N@C_{80}-2D has Sc–N bond lengths of 1.98, 2.04, and 2.05 Å, and Sc–N–Sc angles of 126°, 136°, and 98°, respectively. In addition, the deformation energy (E_d) is 6.60 eV, which is larger than that of the α-Sc_3N@C_{80}-2D phase (6.07 eV). This is mainly due to the greater change in Sc–N bond lengths in a single distorted α'-Sc_3N@C_{80} compared to isolated Sc_3N@C_{80}, resulting in a stronger interaction between Sc_3N and C_{80}. Moreover, the encapsulation of Sc_3N clusters results in weaker inter-cage C–C bonds, reducing the distortion of the Sc_3N@C_{80} cluster, resulting in E_d values of α-Sc_3N@C_{80}-2D and

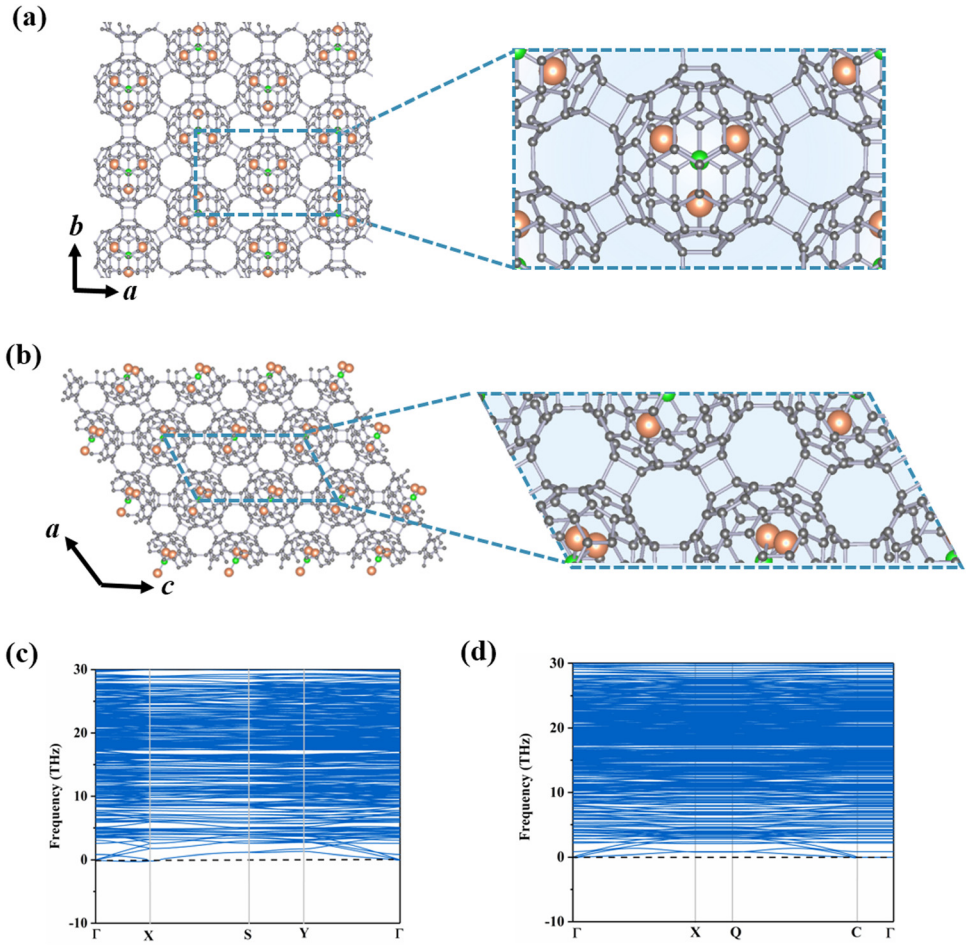

Fig. 2 Crystal structures and phonon dispersions of monolayers (a) and (c) α-$Sc_3N@C_{80}$-2D and (b) and (d) α′-$Sc_3N@C_{80}$-2D, where grey, orange and green denote C, Sc and N atoms.

α′-$Sc_3N@C_{80}$-2D smaller than that of α-C_{80}-2D. And its basal plane is perpendicular to the plane of the α-$Sc_3N@C_{80}$-2D monolayer (Fig. S7(b), ESI†).

Fig. S8 and S9 (ESI†) depict different β-$Sc_3N@C_{80}$-2D monolayers and their respective phonon dispersions. We have observed that the lowest energy β-$Sc_3N@C_{80}$-2D monolayer exhibits imaginary frequencies in the phonon dispersion calculations, suggesting that the Sc_3N cluster cannot be enclosed within β-C_{80}-2D. Taking the imaginary frequency of −1.70 THz at the Γ point as an example, the animation movie reveals complex vibrational modes in the β-$Sc_3N@C_{80}$-2D phase. Specifically, the carbon atoms on the C_{80} cage display two distinct vibration modes: stretching and swinging motions relative to the fullerene center, while the Sc–N bond in the Sc_3N cluster belongs to a stretching–bending vibration mode. In addition, the lowest energy γ-$Sc_3N@C_{80}$-2D crystallizes in the space group *P*1 (No. 1) with lattice parameters a = 10.23 Å and b = 10.67 Å. The embedding of Sc_3N into the γ-C_{80}-2D phase significantly elongates the distance between the two C_{80} fullerenes along the b direction from 1.76 Å to 3.03 Å, surpassing the length of C–C single bonds, as displayed in Fig. S10 (ESI†). Meanwhile, compared to the isolated $Sc_3N@C_{80}$ (Fig. S6(d), ESI†), the deformation energy of the γ-$Sc_3N@C_{80}$ cage is relatively larger. Moreover, the formation energy of this phase is 4.71 eV, signifying an endothermic encapsulation process. Therefore, Sc_3N also cannot stable the γ-C_{80}-2D crystal.

It is important to observe the molecular behavior of metallofullerenes in the crystal lattice. Both previous computational and experimental studies have unraveled that the Sc_3N cluster is freely rotating in single C_{80} fullerene.[46–48] To probe the temperature dependent dynamics of the Sc_3N cluster in α-$Sc_3N@C_{80}$-2D and α′-$Sc_3N@C_{80}$-2D phases, we performed molecular dynamics simulations and used spatial distribution maps to describe the detailed distribution of Sc atoms at the selected temperatures. Fig. 3 and Fig. S11, S12 and animation movies in the ESI† show the trajectories of 2D crystal structures from the AIMD simulation for 10 ps at different temperatures. For α-$Sc_3N@C_{80}$-2D (Fig. 3), the endohedral Sc_3N cluster remains rigidly bonded to the adjacent pentagonal and hexagonal junctions up to 600 K, maintaining a well-ordered structure with the space group *Pma*2 (No. 28). However, as the temperature increases to 800 K, the Sc_3N clusters undergo rotational motion along multiple directions, resulting in the loss of long-range order in the entire system. Such transformation

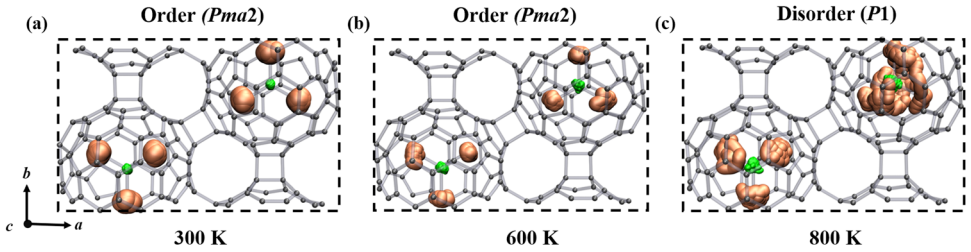

Fig. 3 Schematic representation of order–disorder states of the α-Sc_3N@C_{80}-2D crystal driven by temperature at (a) 300 K, (b) 600 K, and (c) 800 K. The representative rotational operation of the Sc_3N species for the α-Sc_3N@C_{80}-2D phase is available in the movies of the ESI.†

can be considered as a temperature-induced order–disorder transition. In the case of α′-Sc_3N@C_{80}-2D, the Sc_3N clusters exhibit unrestricted rotation at 300 K, inducing a disordered distribution of molecular orientations (Fig. S12, ESI†).

3.C. Electronic structures, carrier mobility, and optical absorption properties

The electronic band structures of α-C_{80}-2D, β-C_{80}-2D, α-Sc_3N@C_{80}-2D, and α′-Sc_3N@C_{80}-2D are plotted in Fig. 4, and the 2D Brillouin region for the four types of crystal lattices is detailed in Fig. S2 (ESI†). One can see that α-C_{80}-2D exhibits a small indirect band behavior with a band gap of 0.14 eV. In other words, the strong C–C bonding interaction (E_b = 2.01 eV) significantly changes the electronic structure of α-C_{80}-2D assembly of semiconducting C_{80} fullerenes. Meanwhile, β-C_{80}-2D still behaves as a semiconductor with a direct band gap of 0.25 eV at point *K*, which is close to the band gap of the freestanding C_{80} cage (0.28 eV), meaning that the coupling strength in such polymerization is relatively weaker (E_b = 1.85 eV). For comparison, the 2D networks of the C_{60} fullerene possess sizeable band gaps of 1.74 and 1.67 eV.[18] Interestingly, the orientation of the Sc_3N clusters in α-C_{80}-2D monolayers has a notable effect on the band structure. Specifically, α-Sc_3N@C_{80}-2D has an indirect band gap of 0.36 eV, and α′-Sc_3N@C_{80}-2D exhibits distinctly different positions of the valence band maximum (VBM) and conduction band minimum (CBM) with an indirect band gap of 0.12 eV. Compared to individual metallofullerene Sc_3N@C_{80}, the band gaps of both α-Sc_3N@C_{80}-2D and α′-Sc_3N@C_{80}-2D phases are greatly reduced, primarily attributed to the inter-cage conjugated interaction. All these results demonstrate that self-assembling can generate richer electronic properties relative to those of individual clusters.

Based on the deformation potential theory,[49,50] the transport properties of semiconducting β-C_{80}-2D, α-Sc_3N@C_{80}-2D, and α′-Sc_3N@C_{80}-2D monolayers are discussed in terms of effective mass and carrier mobility. The detailed results are described in the Supplementary Note 1 of the ESI.† As seen from Table S3 (ESI†), the electron effective masses of β-C_{80}-2D are larger than those of holes, similar to the previously reported α-C_{60}-2D.[19] Owing to the disparities in the dispersion of valence and conduction bands of α-Sc_3N@C_{80}-2D and α′-Sc_3N@C_{80}-2D, significant variations are also observed in their effective masses of electrons and holes. In α-Sc_3N@C_{80}-2D, the effective masses of holes are considerably larger than those of electrons.

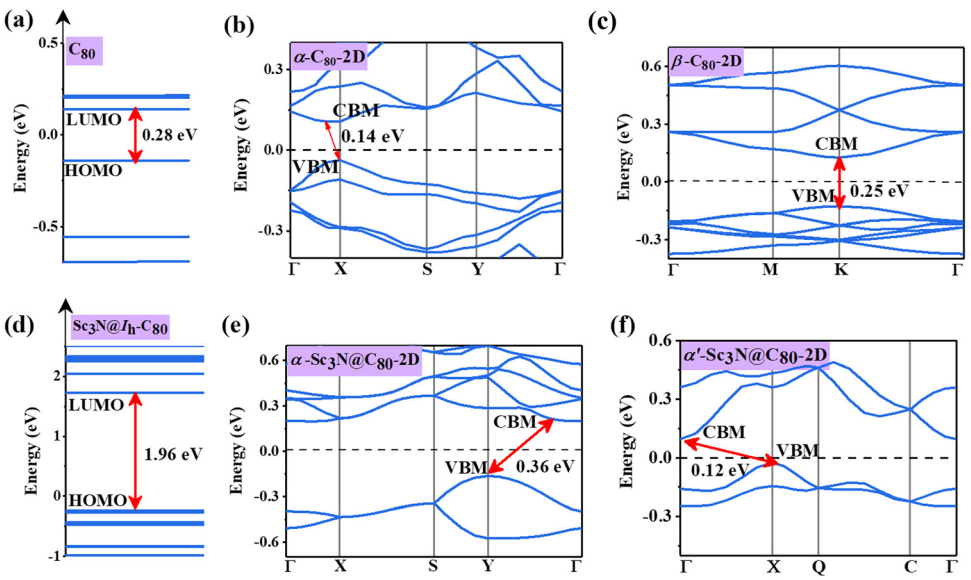

Fig. 4 Electronic structures of (a) C_{80} fullerene, (b) α-C_{80}-2D, (c) β-C_{80}-2D, (d) Sc_3N@I_h–C_{80} fullerene, (e) α-Sc_3N@C_{80}-2D, and (f) α′-Sc_3N@C_{80}-2D. The Fermi level is set to zero.

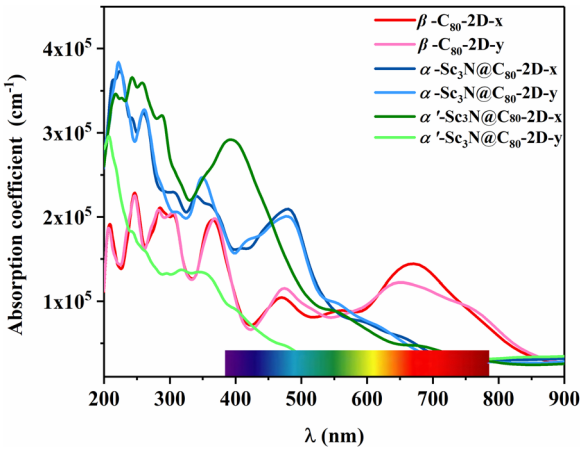

Fig. 5 Optical absorption coefficients of β-C_{80}-2D, α-$Sc_3N@C_{80}$-2D and α'-$Sc_3N@C_{80}$-2D monolayers calculated by the HSE06 functional. The wavelength range of the visible light region (380–780 nm) is in iridescent color.

Conversely, the hole effective masses in α'-$Sc_3N@C_{80}$-2D are smaller than the electron ones. Both the electron and hole effective masses of β-C_{80}-2D are higher than those in α-$Sc_3N@C_{80}$-2D and α'-$Sc_3N@C_{80}$-2D materials. More importantly, the highest carrier mobility obtained in the β-C_{80}-2D monolayer (5.57×10^3 cm^2 V^{-1} s^{-1}) is comparable to those of α-C_{60}-2D (1.24×10^3 cm^2 V^{-1} s^{-1})[19] and black phosphorene (10^3 cm^2 V^{-1} s^{-1}).[51] Such high electron mobility can be ascribed to small effective masses and deformation potential constants of the β-C_{80}-2D monolayer.

To explore potential optoelectronic applications, the absorption spectra of these three 2D semiconductors are simulated and show good absorption intensity from the near-infrared (NIR) to the ultraviolet (UV) regions, suggesting the usage as active layers in solar cells (Fig. 5). In particular, a high absorption coefficient (3.85×10^5 cm^{-1}) is obtained in the ultraviolet region, which is comparable to that of the C_{60} 2D crystal.[52] Such strong ultraviolet absorption capability can not only be utilized in wearable devices to resist ultraviolet radiation and prevent tanning and sunburn, but also holds promise as potential photocatalysts. Excitingly, β-C_{80}-2D exhibits a well-defined strong absorption characteristic in the wavelength range of 600–750 nm. It overcomes the limitation of the low absorption coefficient of conventional carbon nanomaterials in the longer wavelength regime[53,54] and might be useful for future biomedical applications. In addition, for α'-$Sc_3N@C_{80}$-2D, the absorption peak along the x direction is stronger than that along the y direction, suggesting an inherent anisotropic characteristic in light absorption due to the symmetry of the 2D crystal. This phenomenon shows a pronounced linear dichroism and implies potential applications in the design of light detection and new-concept optoelectronic devices.

4. Conclusions

In summary, we have demonstrated that C_{80} and its endohedral derivatives can be used as versatile building blocks to assemble thermodynamically and dynamically stable 2D lattices *via* covalent bonding with each other. Further analysis indicates that the initially unstable pristine C_{80} cages can polymerize into two stable monolayer phases (namely, α-C_{80}-2D and β-C_{80}-2D), because the bond energy released by the [2+2] cycloaddition polymerization of C_{80} is greater than the deformation energy of the corresponding cage. Among them, α-C_{80}-2D exhibits an indirect band behavior, while β-C_{80}-2D is a direct semiconductor with appreciable carrier mobility and strong absorption in the long wave range. By incorporating Sc_3N clusters into each C_{80} cage, we successfully obtain 2D semiconductors of α-$Sc_3N@C_{80}$-2D and α'-$Sc_3N@C_{80}$-2D, which exhibit bistable states with diverse physical properties, such as distinct band structures with bandgaps ranging from 0.36 to 0.12 eV, exceptional electron transport properties with a mobility from 0.31×10^3 cm^2 V^{-1} s^{-1} to 0.17×10^3 cm^2 V^{-1} s^{-1}, broad optical absorption from the near-infrared to ultraviolet regimes, and remarkably strong anisotropic optical adsorption. Furthermore, a temperature-driven order–disorder transition is observed in the α-$Sc_3N@C_{80}$-2D lattice, offering an example of profound insight into the microscopic mechanism of order–disorder phase transition in 2D materials. In a word, such polymeric C_{80} monolayers can act as promising ''host'' materials for diverse endohedral doping, thereby contributing to the development of optical, ferroelectric, ferromagnetic and other functional materials. Furthermore, whether α-$Sc_3N@C_{80}$-2D and α'-$Sc_3N@C_{80}$-2D phases can be transformed through external fields, such as electric fields, photoexcitation, is also worthy of investigation, as this phenomenon holds promise in high-resolution fast data storage and in-memory computing devices.

Author contributions

Yang Zhao: conceptualization, methodology, software, formal analysis, investigation, data curation, writing – original draft, writing – review and editing, and visualization; Yu Guo: formal analysis and funding acquisition; Yanyan Zhao: formal analysis; Xueke Yu: writing – review and editing; Nikolai Cherenda: writing – review and editing and funding acquisition; Yan Su and Jijun Zhao: conceptualization, software, resources, writing – review and editing, and funding acquisition. All authors have read and agreed to the published version of the manuscript.

Conflicts of interest

There are no conflicts to declare.

Acknowledgements

This work was supported by the National Natural Science Foundation of China (91961204 and 12174045), the Fundamental Research Funds for the Central Universities (DUT22RC(3)009), and the financial support of our International Cooperative Project (ICR2304). The computational resources utilized in this research

were provided by the Supercomputing Center of the Dalian University of Technology and Shanghai Supercomputer Center.

References

1 H. W. Kroto, J. R. Heath, S. C. O'Brien, R. F. Curl and R. E. Smalley, *Nature*, 1985, **318**, 162.
2 W. Krätschmer, L. D. Lamb, K. Fostiropoulos and D. R. Huffman, *Nature*, 1990, **347**, 354.
3 J. W. Arbogast and C. S. Foote, *J. Am. Chem. Soc.*, 1991, **113**, 8886.
4 D. H. Parker, P. Wurz, K. Chatterjee, K. R. Lykke, J. E. Hunt, M. J. Pellin, J. C. Hemminger, D. M. Gruen and L. M. Stock, *J. Am. Chem. Soc.*, 1991, **113**, 7499.
5 Y. Chai, T. Guo, C. Jin, R. E. Haufler, L. P. F. Chibante, J. Fure, L. Wang, J. M. Alford and R. E. Smalley, *J. Phys. Chem.*, 1991, **95**, 7564.
6 J. R. Heath, S. C. O'Brien, Q. Zhang, Y. Liu, R. F. Curl, F. K. Tittel and R. E. Smalley, *J. Am. Chem. Soc.*, 1985, **107**, 7779.
7 A. A. Popov, S. Yang and L. Dunsch, *Chem. Rev.*, 2013, **113**, 5989.
8 S. Stevenson, G. Rice, T. Glass, K. Harich, F. Cromer, M. R. Jordan, J. Craft, E. Hadju, R. Bible, M. M. Olmstead, K. Maitra, A. J. Fisher, A. L. Balch and H. C. Dorn, *Nature*, 1999, **401**, 55.
9 K. Zhang, C. Wang, M. Zhang, Z. Bai, F.-F. Xie, Y.-Z. Tan, Y. Guo, K.-J. Hu, L. Cao, S. Zhang, X. Tu, D. Pan, L. Kang, J. Chen, P. Wu, X. Wang, J. Wang, J. Liu, Y. Song, G. Wang, F. Song, W. Ji, S.-Y. Xie, S.-F. Shi, M. A. Reed and B. Wang, *Nat. Nanotechnol.*, 2020, **15**, 1019.
10 J. Li, S. Hou, Y.-R. Yao, C. Zhang, Q. Wu, H.-C. Wang, H. Zhang, X. Liu, C. Tang, M. Wei, W. Xu, Y. Wang, J. Zheng, Z. Pan, L. Kang, J. Liu, J. Shi, Y. Yang, C. J. Lambert, S.-Y. Xie and W. Hong, *Nat. Mater.*, 2022, **21**, 917.
11 Y. Zhao, Y. Guo, Y. Qi, X. Jiang, Y. Su and J. Zhao, *Adv. Sci.*, 2023, 2301265.
12 L. Li, M. Zhen, H. Wang, Z. Sun, W. Jia, Z. Zhao, C. Zhou, S. Liu, C. Wang and C. Bai, *Nano Lett.*, 2020, **20**, 4487.
13 X. Li, M. Zhen, C. Zhou, R. Deng, T. Yu, Y. Wu, C. Shu, C. Wang and C. Bai, *ACS Nano*, 2019, **13**, 8597.
14 A. R. Puente Santiago, T. He, O. Eraso, M. A. Ahsan, A. N. Nair, N. Chava, T. Zheng, S. Pilla, O. Fernandez-Delgado, A. Du, S. T. Sreenivasan and L. Echegoyen, *J. Am. Chem. Soc.*, 2020, **142**, 17923.
15 L. Hou, X. Cui, B. Guan, S. Wang, R. Li, Y. Liu, D. Zhu and J. Zheng, *Nature*, 2022, **606**, 507.
16 F. Pan, K. Ni, T. Xu, H. Chen, Y. Wang, K. Gong, C. Liu, X. Li, M.-L. Lin, S. Li, X. Wang, W. Yan, W. Yin, P.-H. Tan, L. Sun, D. Yu, R. S. Ruoff and Y. Zhu, *Nature*, 2023, **614**, 95.
17 E. Meirzadeh, A. M. Evans, M. Rezaee, M. Milich, C. J. Dionne, T. P. Darlington, S. T. Bao, A. K. Bartholomew, T. Handa, D. J. Rizzo, R. A. Wiscons, M. Reza, A. Zangiabadi, N. Fardian-Melamed, A. C. Crowther, P. J. Schuck, D. N. Basov, X. Zhu, A. Giri, P. E. Hopkins, P. Kim, M. L. Steigerwald, J. Yang, C. Nuckolls and X. Roy, *Nature*, 2023, **613**, 71.
18 B. Peng, *J. Am. Chem. Soc.*, 2022, **144**, 19921.
19 L. Yu, J. Xu, B. Peng, G. Qin and G. Su, *J. Phys. Chem. Lett.*, 2022, **13**, 11622.
20 W. Li, R. Yang and M. Sun, *J. Mater. Chem. A*, 2023, **11**, 3949.
21 S. Zhao, X. Zhang, Y. Ni, Q. Peng and Y. Wei, *Carbon*, 2023, **202**, 118.
22 H. W. Kroto, *Nature*, 1987, **329**, 529.
23 A. R. Khamatgalimov and V. I. Kovalenko, *Fullerenes, Nanotubes Carbon Nanostruct.*, 2011, **19**, 599.
24 C. Zhao, K. Tan, M. Nie, Y. Lu, J. Zhang, C. Wang, X. Lu and T. Wang, *Inorg. Chem.*, 2020, **59**, 8284.
25 T. Wang and C. Wang, *Acc. Chem. Res.*, 2014, **47**, 450.
26 Y. Feng, T. Wang, J. Wu, Z. Zhang, L. Jiang, H. Han and C. Wang, *Chem. Commun.*, 2014, **50**, 12166.
27 R. Valencia, A. Rodríguez-Fortea, S. Stevenson, A. Balch and L. J. M. Poblet, *Inorg. Chem.*, 2009, **48**, 5957.
28 B. Q. Mercado, M. M. Olmstead, C. M. Beavers, M. L. Easterling, S. Stevenson, M. A. Mackey, C. E. Coumbe, J. D. Phillips, J. P. Phillips, J. M. Poblet and A. L. Balch, *Chem. Commun.*, 2010, **46**, 279.
29 G. Kresse and J. Furthmüller, *Phys. Rev. B: Condens. Matter Mater. Phys.*, 1996, **54**, 11169.
30 G. Kresse and J. Furthmüller, *Comput. Mater. Sci.*, 1996, **6**, 15.
31 J. P. Perdew, K. Burke and M. Ernzerhof, *Phys. Rev. Lett.*, 1996, **77**, 3865.
32 G. Kresse and D. Joubert, *Phys. Rev. B: Condens. Matter Mater. Phys.*, 1999, **59**, 1758.
33 V. I. Anisimov, J. Zaanen and O. K. Andersen, *Phys. Rev. B: Condens. Matter Mater. Phys.*, 1991, **44**, 943.
34 A. Rohrbach, J. Hafner and G. Kresse, *J. Phys.: Condens. Matter*, 2003, **15**, 979.
35 S. L. Dudarev, G. A. Botton, S. Y. Savrasov, C. J. Humphreys and A. P. Sutton, *Phys. Rev. B: Condens. Matter Mater. Phys.*, 1998, **57**, 1505.
36 M. Musa Saad H-E, *Bull. Mater. Sci.*, 2022, **45**, 69.
37 J. Heyd, G. E. Scuseria and M. Ernzerhof, *J. Chem. Phys.*, 2003, **118**, 8207.
38 G. Kresse and J. Hafner, *Phys. Rev. B: Condens. Matter Mater. Phys.*, 1993, **47**, 558.
39 A. Togo and I. Tanaka, *Scr. Mater.*, 2015, **108**, 1.
40 A. R. Khamatgalimov, A. V. Luzhetskii and V. I. Kovalenko, *Int. J. Quantum Chem.*, 2008, **108**, 1334.
41 R. Nakanishi, J. Satoh, K. Katoh, H. Zhang, B. K. Breedlove, M. Nishijima, Y. Nakanishi, H. Omachi, H. Shinohara and M. Yamashita, *J. Am. Chem. Soc.*, 2018, **140**, 10955.
42 S. Sato, S. Seki, G. F. Luo, M. Suzuki, J. Lu, S. Nagase and T. Akasaka, *J. Am. Chem. Soc.*, 2012, **134**, 11681.
43 K. Jayanand, S. Chugh, N. Adhikari, M. Min, L. Echegoyen and A. B. Kaul, *J. Mater. Chem. C*, 2020, **8**, 3970.
44 J. R. Pinzon, M. E. Plonsk-Brzezinska, C. M. Cardona, A. J. Athans, S. S. Gayathri, D. M. Guldi, M. Á. Herranz, N. Martín, T. Torres and L. Echegoyen, *Angew. Chem., Int. Ed.*, 2008, **47**, 4173.
45 Y. Chai, X. Liu, B. Wu, L. Liu, Z. Wang, Y. Weng and C. Wang, *J. Am. Chem. Soc.*, 2020, **142**, 4411.

46 A. A. Popov and L. Dunsch, *J. Am. Chem. Soc.*, 2008, **130**, 17726.
47 T. Heine, K. Vietze and G. Seifert, *Magn. Reson. Chem.*, 2004, **42**, S199.
48 Y. Hao, Y. Wang, L. Spree and F. Liu, *Inorg. Chem. Front.*, 2021, **8**, 122.
49 S. Takagi, A. Toriumi, M. Iwase and H. Tango, *Electron Devices*, 1994, **41**, 2357.
50 S. Bruzzone and G. Fiori, *Appl. Phys. Lett.*, 2011, **99**, 222108.
51 J. Qiao, X. Kong, Z. X. Hu, F. Yang and W. Ji, *Nat. Commun.*, 2014, **5**, 4475.
52 R. M. Tromer, L. A. Ribeiro and D. S. Galvão, *Chem. Phys. Lett.*, 2022, **804**, 139925.
53 X. Wang, L. Cao, S. T. Yang, F. S. Lu, M. J. Meziani, L. Tian, K. W. Sun, M. A. Bloodgood and Y. P. Sun, *Angew. Chem., Int. Ed.*, 2010, **49**, 5310.
54 P. Anilkumar, L. Cao, J. J. Yu, K. N. Tackett, P. Wang, M. J. Meziani and Y. P. Sun, *Small*, 2013, **9**, 545.